Volume 28
Number 5
4 February 2026
Pages 3143–3762

PCCP

Physical Chemistry Chemical Physics

rsc.li/pccp

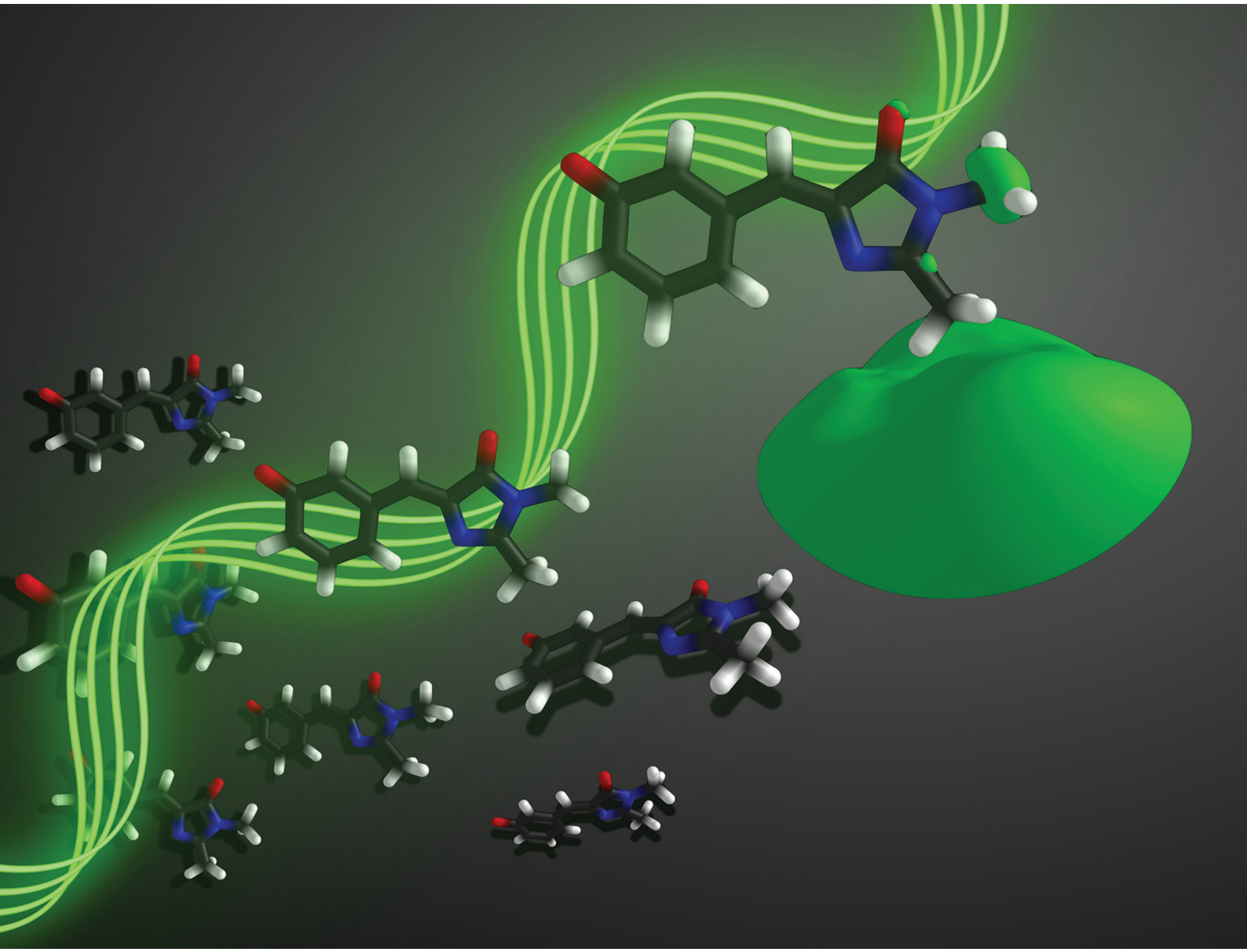

ISSN 1463-9076

ROYAL SOCIETY OF CHEMISTRY

PAPER

Anne P. Rasmussen *et al.*

Dipole-bound states in the *meta* form of the green fluorescent protein chromophore observed by cryogenic action spectroscopy

PCCP Owner Societies

PCCP

ROYAL SOCIETY OF CHEMISTRY

PAPER

View Article Online
View Journal | View Issue

Cite this: *Phys. Chem. Chem. Phys.*, 2026, **28**, 3168

Dipole-bound states in the *meta* form of the green fluorescent protein chromophore observed by cryogenic action spectroscopy

Anne P. Rasmussen, *[ab] Nikolaj Klinkby [a] and Lars H. Andersen [a]

Received 10th December 2025,
Accepted 8th January 2026

DOI: 10.1039/d5cp04796j

rsc.li/pccp

We report the observation of states arising from the interaction of an excess electron with the dipole moment of a biochromophore, the *meta* form of the green fluorescent protein (GFP) model chromophore *p*-hydroxybenzylidene-2,3-dimethylimidazolinone (mHBDI), using cryogenic ion action spectroscopy. Distinct spectral features appear in the 19 400–20 100 cm^{-1} region near the electron detachment threshold of mHBDI. Dipole-bound (DBS) and dipole-resonance (DRS) states are identified below and above the detachment energy, respectively. The vertical detachment energy is determined to be 19 620 cm^{-1}. The DBS-band origin is at 19 444 cm^{-1} with a binding energy of 176 cm^{-1}. Complementary DFT (ωB97X-D/aug-cc-pVTZ) calculations provide insight into the structure and vibrational resonances of the excess electron in this biologically relevant chromophore. The results extend the understanding of dipole-bound and resonance states in complex molecular systems. We find that one low-energy mode of the neutral radical is particularly Franck–Condon active. The same mode has previously been found to dominate absorption spectra of other GFP-chromophore derivatives. It is suggested that the DRSs are potential doorway states for capture of low energy electrons.

1. Introduction

Non-valence-bound states (NBSs) are anionic states in which an excess electron is weakly bound to a neutral molecule through interactions that extend well beyond the range of valence orbitals.[1–4] NBSs have been found in molecular anions relevant in a range of different fields, from atmospheric chemistry[5,6] or astrophysics[7–10] to biology.[11–14]

The most common type of NBS is the dipole-bound state (DBS), which can form when a neutral molecule possesses a sufficiently large dipole moment to support an electron bound below the detachment threshold.[2,3,15,16] A theoretical lower limit for the dipole moment required to support a DBS is approximately 1.6 D,[2,17] while, in practice, dipole-bound states are typically observed only for molecules with dipole moments greater than about 2.5 D.[2,16] DBSs were first identified as resonances in the photodetachment spectrum of enolate anions,[18–20] and have since been reported for a wide variety of molecular anions.

While the dipole potential typically gives the strongest electron binding, higher-order contributions can also provide binding, as for quadrupole-bound states[4,21] and correlation-bound states.[22–24] These interactions all act over distances much larger than typical valence-bond lengths, although decaying more rapidly with distance than the Coulomb potential. The binding energy of the excess electron in these nonvalence-bound states is therefore generally small, resulting in highly diffuse electronic wavefunctions.

Dipole-bound states typically occur within a narrow energy window just below the electron-detachment threshold. When nuclear vibrational energy is present in the molecular core—for example, at finite temperature—the total energy can exceed the energy for electron-detachment, and the states manifest as autodetaching dipole-resonance states (DRSs) in the continuum.[14] Dipole-resonance states are thus analogous to dipole-bound states, except that they possess sufficient nuclear energy to eject a loosely dipole-bound electron through non–Born–Oppenheimer coupling between electronic and nuclear motions *i.e.* through vibrational autodetachment.

DBSs are relevant in the field of photoactive proteins and biomolecules, as they have been suggested to be a 'doorway' for the formation of valence-bound anions.[25–27] In particular, DBSs and DRSs were detected in two anionic model chromophores of the Photoactive Yellow Protein (PYP).[13,14] PYP is a bacterial photoreceptor involved in the negative phototaxis response of Halorhodospira halophila[28,29] and two model-chromophores have received recent attention in connection with DBS, the

[a] *Department of Physics and Astronomy, Aarhus University, Aarhus 8000, Denmark. E-mail: apr@phys.au.dk, lha@phys.au.dk*
[b] *Université Paris-Saclay, CNRS, Institut des Sciences Moléculaires d'Orsay, 91405 Orsay, France*

deprotonated *para*-coumaric acid with a methyl ester group, pCE^-, and its ketone derivative, pCK^-.[14] Another important photoactive protein is the Green Fluorescent Protein (GFP), which is widely used as a biomarker within biological and life sciences due to its characteristic green bioluminescence.[30–33] The most commonly used model-chromophore of GFP is the deprotonated *p*-hydroxybenzylidene-2,3-dimethylimidazolinone ($pHBDI^-$).[34] Studying the photophysics of these chromophores in isolation (*i.e.* gas phase) is important to understand the influence of the protein environment and to benchmark theory.

The photo-physical properties of $pHBDI^-$ have been extensively studied in the gas phase,[35–40] yet so far no DBSs have been detected for pHBDI, even though the dipole moment of the neutral radical core has been calculated to be about 7 D,[41] well above the $|\mu| > 2.5$ D limit to support DBSs. The $pHBDI^-$ has a bright $S_0 \rightarrow S_1$ absorption that extends over the detachment-energy threshold. Since the weakly bound DBSs and DRSs only exist in a narrow energy range close to the detachment threshold they are difficult to identify spectroscopically when many strong valence transitions exist in the same energy region. Moving the oxygen atom on the phenolate ring from the *para* to the *meta* position leads to pronounced spectroscopic changes.[42] In *meta*-$HBDI^-$ ($mHBDI^-$), the $S_0 \rightarrow S_1$ transition is red-shifted to about 700 nm, well under the detachment threshold, and it becomes optically dark due to its charge-transfer character.[42] This makes it an excellent system for studying dipole-type resonances near the detachment threshold without interference from valence-bound states.

Detecting subtle dipole-bound/resonance states in molecular anions has been challenging due to experimental limitations. We overcome these challenges using a novel action–absorption approach combining a cryogenic ion trap with an ion-storage ring,[43] revealing DBSs previously inaccessible.[44] Here, we report the gas-phase action–absorption spectrum of $mHBDI^-$, with DBSs and DRSs near the electron-detachment threshold. Quantum chemical calculations at the ωB97X-D/aug-cc-pVTZ[45,46] level of theory support the observations, demonstrating the power of cryogenic trapping and ion-storage-ring spectroscopy to uncover new electronic states in bio-chromophores.

2. Methods

The setup, which has previously been described,[38,43,47,48] is illustrated in Fig. 1. Briefly, chromophore ions are continuously produced in an electrospray-ionization source and accumulated in a 16-pole radio frequency (RF) ion trap. After accumulating for 200 ms, the ions are released as a bunch and accelerated to 4 keV. A magnet is used to mass-to-charge select the relevant ions. The ions are then slowed down and trapped in another 16-pole RF trap. This trap is cooled to 6 K by a liquid helium cryo-cooler system, and cooled He-buffer gas is introduced to cool the ions. The ions are cooled for 150 ms, again accelerated

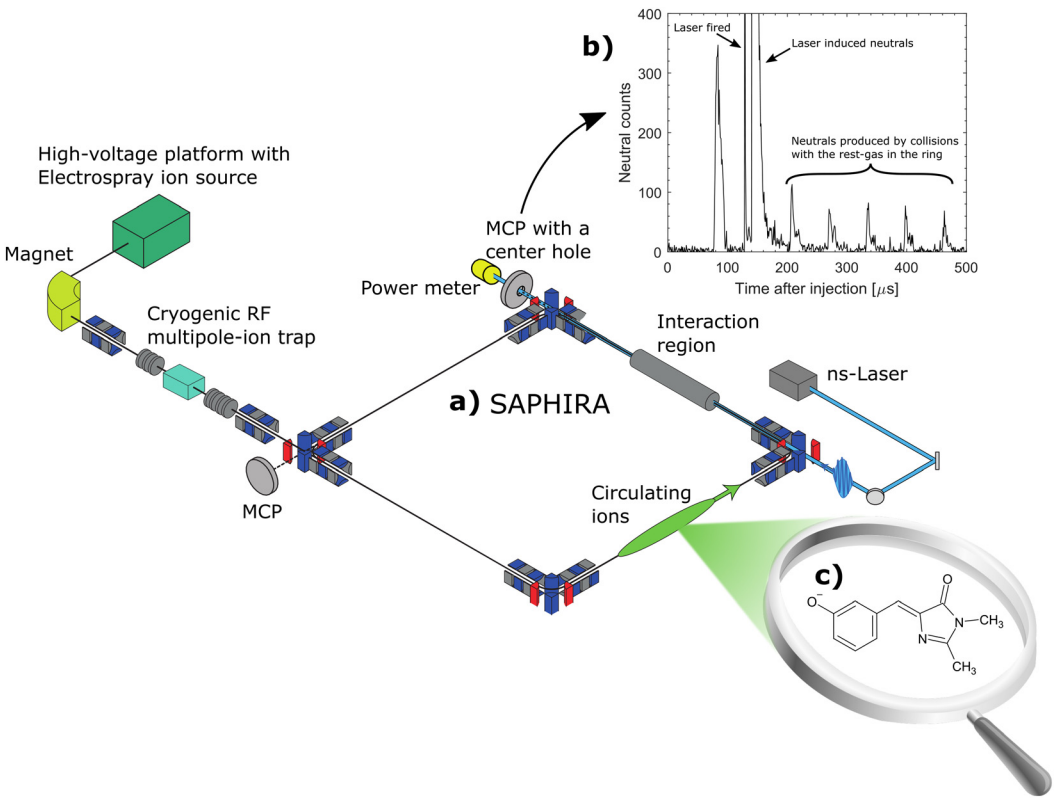

Fig. 1 (a) The SAPHIRA ion-storage ring. The ion source, detectors and laser system are shown schematically. The ions are irradiated in the interaction region and neutral particles are counted after the interaction region by two separately located MCP detectors. (b) A histogram of neutral counts as a function of time after injection measured on the prompt detector. (c) Molecular structure of deprotonated mHBDI (mass 215 amu).

to 4 keV and finally injected into the ring. Ions are accumulated in the first trap while the previous bunch of ions is simultaneously cooled in the cold trap, resulting in a duty cycle of 5 Hz. The ring is held at room temperature at a pressure of $\sim 10^{-9}$ mbar.

A nano-second laser is used to excite the ions in the interaction region (see Fig. 1b) during their second revolution in the ring, before the ions have time to heat up either by collisions with the residual gas or through black-body radiation.[38,43] When addressing bound excited states, resonant two-photon excitation results in prompt electron emission rendering a detectable neutral product.[44] Above the detachment limit, neutrals are in addition produced from non-adiabatic vibrational auto-detachment.[38] Neutral detection is achieved using a microchannel plate (MCP) detector positioned behind the interaction region. The detector features a central hole that allows laser-light monitoring with a downstream power meter. A second MCP, placed at the end of the last straight section of the ring, records neutrals produced after the ions have passed the corner, which for mHBDI occurs approximately 10 μs after photo excitation. At the end of the measurement cycle, the remaining ions are dumped on the second MCP to measure the total ion count. The action–absorption spectrum is generated by counting the number of neutrals created as a function of wavelength (λ) and normalizing to the number of ions and photons as

$$\text{Signal}\,(\lambda) = \frac{N(\lambda)}{N_0 \cdot N_\lambda} \qquad (1)$$

where $N(\lambda)$ is the number of neutrals detected at wavelength λ, N_0 is the number of ions dumped on the second MCP, and N_λ is the number of photons calculated from the laser-pulse energy and the wavelength.

3. Results

The measured action–absorption spectrum of $mHBDI^-$ is shown in Fig. 2. Panel (a) presents the full spectrum, while panel (b) highlights a narrow region exhibiting distinct spectral features near the electron-detachment limit. Previous photoelectron spectroscopy studies have placed the vertical detachment energy (VDE) in the range of (2.4–2.54) ± 0.1 eV (19 360–20 490 cm^{-1}), with the spread attributed to inhomogeneous broadening caused by internal rotation along single C–C bonds in the ground state.[42] The action signal shown in Fig. 2a rises significantly in this threshold region, and we assign the VDE to 19 620 ± 20 cm^{-1}, corresponding to the onset of the non-resonant background (see Fig. 2b and the SI for details).

The $mHBDI^-$ is predicted to possess a dark S_1 charge-transfer state at around 14 250 cm^{-1} with a very low oscillator strength.[42] Consequently, the S_1 state does not contribute to the action signal observed in the 19 400–20 100 cm^{-1} region. Moreover, the S_2 state, located near 25 000 cm^{-1}, lies well above the energy range considered here. The neutral mHBDI radical has a dipole moment that exceeds the ~2.5 D threshold required to support dipole-bound states. Given that only a single isomer is present in the experiment, the spectral features observed below the VDE are assigned to DBSs, while the features just above the VDE, extending up to 20 100 cm^{-1}, are assigned to DRSs (more discussion below). The distinct resonance structures are hence related to the vibrations of the neutral radical core molecule.

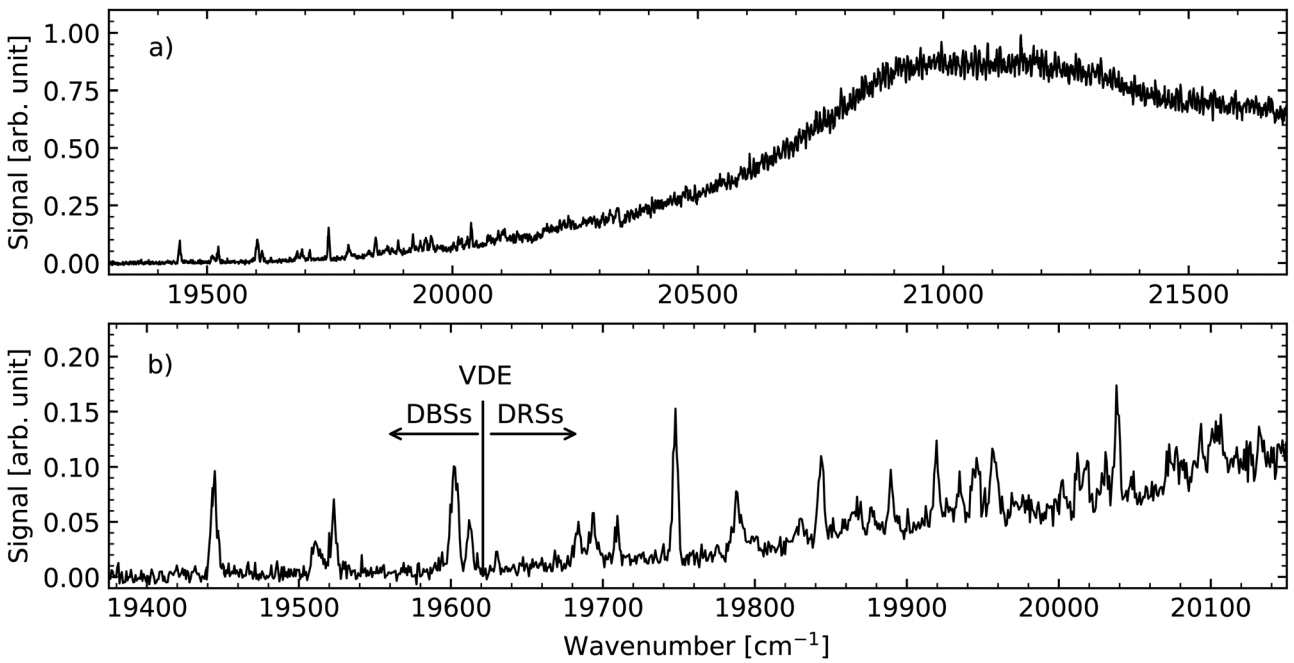

Fig. 2 (a) Action-absorption spectrum of the deprotonated mHBDI. (b) Narrow view of the action-absorption spectrum to show the dipole-bound states (DBSs) and dipole-resonance states (DRSs), below and above the electronic continuum, respectively. The vertical black line indicates the experimentally determined vertical detachment energy (VDE) of 19 620 cm^{-1}, with DBSs below the VDE and DBRs above.

With a band origin of 19 444 cm^{-1} and VDE of 19 620 cm^{-1} the binding energy of the lowest DBS is 176 cm^{-1}. This binding energy is within the usual range found for DBSs (40–200 cm^{-1}).[14,49–51]

No delayed action was observed on the second MCP detector, so all action occurred faster than the approximately 10 μs it takes the ions to pass the corner of the ring and enter into the subsequent straight sections. The same observation was also made for phenoxide, although some resonances (DRSs) were observed to decay on a microsecond time scale for this particular system.[44] Vibrational autodetachment on a picosecond time scale[52] has also been reported.

Table 1 lists the relative energies (E_{rel}) of the four stable isomers of $mHBDI^-$ (see Fig. S2), as well as the calculated adiabatic and vertical detachment energies (ADE, VDE), and the dipole moments of the radical neutral. The ADEs were calculated as the energy differences between the anion and radical neutral at their respective optimized geometries, including zero-point energy (ZPE) corrections, while the VDEs were obtained as the energy difference between the anion and the radical neutral, both at the anion's optimized geometry. Details for the calculations and the vibronic spectra of each of the four isomers are shown in the SI (Fig. S3). The ADEs and VDEs are almost isomer-independent (identical within a few hundred wavenumbers), but the energy of the two E-isomers is significantly higher than for the two Z-isomers. From the relative energies, we expect a ratio of 100 : 23 for Z1 : Z2, assuming a 300 K Boltzmann distribution followed by rapid cooling and kinetic trapping.

The vibronic spectrum was calculated using the Franck–Condon method as implemented in the Gaussian 16 program package.[53] The ground state of the anion (S_0) was taken as the initial state, and the neutral ground state (D_0) as the final state, since DBSs do not significantly influence the structure of the neutral core. Geometry optimizations and vibrational frequency calculations were performed at the ωB97X-D/aug-cc-pVTZ level of theory.[45,46] The simulated spectrum was generated at 6 K. The calculated frequencies of the stick spectrum were scaled by 0.9566[54] and convoluted with a Gaussian line shape having a full width at half maximum (FWHM) of 4 cm^{-1}.

Fig. 3a compares the measured and calculated spectra. The theoretical spectrum was shifted by 512 cm^{-1} so that the calculated band origin coincides with the lowest observed peak. While the DFT calculations reproduce several prominent features of the experimental spectrum, numerous bands remain unassigned. This discrepancy may arise from the limitations of the theoretical model or from the presence of multiple isomers. The DBSs are very diffuse states, which can be a challenge for DFT, even when using a basis set with diffuse functions. For other smaller systems, couple cluster (CCSD) and equation-of-motion-CCSD (EOM-CCSD) have been used to describe the DBSs.[44,55,56] However, this is not feasible with a molecule of this size and is not done in the present study. Different isomers can form during the room-temperature electrospray process and become kinetically trapped upon cryogenic cooling. Similar behavior has been reported for other biomolecular anions produced *via* electrospray ionization and subsequently cooled to cryogenic temperatures.[57–59]

Table 1 Calculated energies of each of the mHBDI isomers at the ωB97X-D/aug-cc-pVTZ[45,46] level of theory

	E_{rel} [cm^{-1}]	ADE [cm^{-1}]	VDE [cm^{-1}]	$\|\mu\|$ [D]
Z1	0	18 932	19 903	7.70
Z2	311	18 806	19 682	3.54
E1	1203	18 866	19 881	6.81
E2	2007	18 422	19 337	5.62

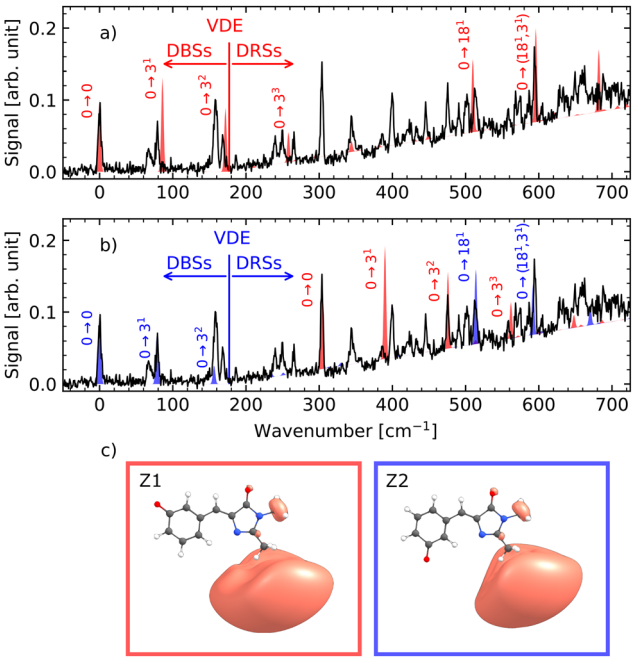

Fig. 3 Narrow view of the action-absorption spectrum where the energy is relative to the DBS-band origin (the lowest-energy peak at 19 444 cm^{-1}). The calculated vibronic spectra are plotted as colored areas. (a) The vibronic spectrum for the Z1 isomer (red) shifted to match the DBS origin. (b) The vibronic spectra of both the Z1 (red) and Z2 (blue) isomers. Here, the Z2 isomer is shifted to the DBS origin, and the Z1 isomer is shifted to match the peak at 304 cm^{-1} (photon energy 19 748 cm^{-1}). For both isomers, the in-plane bending mode (third mode) is particular active in the calculated FC spectra. (c) Calculated DBS electronic orbital for the Z1 and Z2 isomers with an iso-surface value of 0.008.

Fig. 3b shows the experimental spectrum together with calculated vibronic spectra of the two lowest isomers; Z1 and Z2. Based on the order of the calculated VDEs we here assign the first resonances at 19 444 cm^{-1} to be the band origin of the Z2 isomers, and the 19 748 cm^{-1} peak to be that of the Z1 isomer (see Fig. 2b). A shift of 816 cm^{-1} and 638 cm^{-1} is given to the calculated spectrum of Z1 and Z2, respectively to fit the experimental spectrum. Each spectrum is scaled so that the height of its band origin fits the experimental spectrum, and a linear background starting from the VDE is given to the calculated spectrum to account for the direct detachment signal. Only the lowest lying threshold (VDE) belonging to the Z2 isomer is visible in the spectrum. Even with the inclusion of the vibronic spectra of two isomers, many peaks remain unexplained. This may be due to the level of theory used, and further

studies with a higher level of theory will be needed to disentangle the spectrum fully.

The Z1 and Z2 isomers of the neutral radical each exhibit an active bending vibration of the central bridge moiety (Fig. S6), which dominates their spectra. This mode appears at 90 cm^{-1} and 82 cm^{-1} for Z1 and Z2, respectively (see SI). An equivalent mode is also active in $pHBDI^-$ at 80 cm^{-1} (ref. 38) and in *ortho*-$HBDI^-$ at 98 cm^{-1}.[59] In $pHBDI^-$, the active mode persists over about 1500 cm^{-1}, making it one of the most prominent features of its spectrum.[38] In contrast, the lowest-energy modes of $mHBDI^-$ (near 30 and 60 cm^{-1}) are not observed in the present spectrum, although it is noteworthy that their harmonics coincide closely with the $\sim$90 cm^{-1} feature.

In low-energy electron–molecule scattering, a molecule can transiently capture an incoming electron into a dipole-resonance state (DRS) when the electron's kinetic energy is used to excite low-energy vibrational modes and the neutral molecule has a sufficiently large dipole moment. The resonance state will ordinarily autodetach unless it is stabilized. Stabilization can occur through internal conversion (IC), where the excess electronic energy is transferred non-radiatively into molecular vibrations and subsequently redistributed *via* intramolecular vibrational redistribution (IVR), or through radiative decay. These processes can channel population from the dipole-bound electronic resonance state into vibrationally hot levels of the anion, effectively trapping the electron and suppressing autoionization. The scattering outcome is governed by the competition of rates: autodetachment *versus* stabilization (IC/IVR/radiative/collisional). In this work, we have shown that there exist relevant dipole-bound–type resonance states in $mHBDI^-$ just above the continuum limit, associated with low-energy vibrations of the radical core. These states were probed here *via* photoexcitation, but they could equally be populated in a scattering event with a free electron interacting with a dipolar molecule, acting as a doorway for electron capture.

4. Conclusions

This work presents the observation of non-valence bound states (NBSs) in a *meta*-derivative of the GFP model chromophore ($mHBDI^-$), using cryogenic action spectroscopy. These NBSs appear in the 19 400–20 100 cm^{-1} region around the detachment threshold and are attributed to dipole-bound states (DBSs) below the detachment energy and dipole-resonance states (DRSs) above it. The band origin is found at 19 444 cm^{-1}, and the detachment energy is determined to be 19 620 cm^{-1}, yielding a binding energy of 176 cm^{-1} for the lowest DBS of $mHBDI^-$. Importantly, our work reveals the presence of unbound dipolar resonance states that may act as doorway states for electron capture in scattering processes involving dipolar (bio)molecules.

The experimental spectra were complemented by quantum-chemical calculations at the DFT ωB97X-D/aug-cc-pVTZ[45,46] level of theory. While the calculations reproduce several prominent features—particularly those associated with the ν_3 vibration- a precise assignment of all observed peaks requires a higher level of theory. This underscores the need for more advanced theoretical treatments to fully characterize the role of NBSs in biologically relevant chromophores.

Conflicts of interest

There are no conflicts to declare.

Data availability

The data supporting this article have been included as part of the supplementary information (SI). Supplementary information is available. See DOI: https://doi.org/10.1039/d5cp04796j.

Acknowledgements

This work was supported by a research grant (VIL71404) from VILLUM FONDEN.

References

1 E. Fermi and E. Teller, *Phys. Rev.*, 1947, **72**, 399–408.
2 K. D. Jordan and F. Wang, *Annu. Rev. Phys. Chem.*, 2003, **54**, 367–396.
3 J. Simons, *J. Chem. Phys. A*, 2008, **112**, 6401–6511.
4 D. H. Kang and S. K. Kim, *Chem. Phys. Rev.*, 2024, **5**, 041301.
5 Y. Albeck, K. G. Lunny, Y. Benitez, A. J. Shin, D. Strasser and R. E. Continetti, *Angew. Chem.*, 2019, **131**, 5366–5369.
6 Y.-R. Zhang, D.-F. Yuan and L.-S. Wang, *J. Chem. Phys. Lett.*, 2022, **13**, 11481–11488.
7 F. Güthe, M. Tulej, M. V. Pachkov and J. P. Maier, *Astrophys. J.*, 2001, **555**, 466.
8 T. J. Millar, C. Walsh and T. A. Field, *Chem. Rev.*, 2017, **117**, 1765–1795.
9 B. A. Laws, Z. D. Levey, T. W. Schmidt and S. T. Gibson, *J. Am. Chem. Soc.*, 2021, **143**, 18684–18692.
10 J. N. Bull, C. S. Anstoter, M. H. Stockett, C. J. Clarke, J. A. Gibbard, E. J. Bieske and J. R. Verlet, *J. Chem. Phys. Lett.*, 2021, **12**, 11811–11816.
11 J. N. Bull, C. W. West and J. R. Verlet, *Chem. Sci.*, 2016, **7**, 5352–5361.
12 E. Matthews and C. E. Dessent, *J. Chem. Phys. Lett.*, 2018, **9**, 6124–6130.
13 J. N. Bull, C. S. Anstöter and J. R. Verlet, *Nat. Commun.*, 2019, **10**, 5820.
14 L. H. Andersen, A. P. Rasmussen, H. B. Pedersen and N. Klinkby, *Phys. Rev. A*, 2025, **112**, 022821.
15 C. Desfrançois, H. Abdoul-Carime, N. Khelifa and J. Schermann, *Phys. Rev. Lett.*, 1994, **73**, 2436.
16 C.-H. Qian, G.-Z. Zhu and L.-S. Wang, *J. Chem. Phys. Lett.*, 2019, **10**, 6472–6477.
17 J.-M. Lévy-Leblond, *Phys. Rev.*, 1967, **153**, 1–4.
18 A. H. Zimmerman and J. I. Brauman, *J. Chem. Phys.*, 1977, **66**, 5823–5825.

19 K. R. Lykke, R. D. Mead and W. Lineberger, *Phys. Rev. Lett.*, 1984, **52**, 2221.
20 R. D. Mead, K. R. Lykke, W. Lineberger, J. Marks and J. I. Brauman, *J. Chem. Phys.*, 1984, **81**, 4883–4892.
21 M. Gutowski, P. Skurski, X. Li and L.-S. Wang, *Phys. Rev. Lett.*, 2000, **85**, 3145.
22 S. Klaiman, E. V. Gromov and L. S. Cederbaum, *J. Chem. Phys. Lett.*, 2013, **4**, 3319–3324.
23 V. K. Voora and K. D. Jordan, *Nano Lett.*, 2014, **14**, 4602–4606.
24 J. N. Bull and J. R. Verlet, *Sci. Adv.*, 2017, **3**, e1603106.
25 A. Kunin and D. M. Neumark, *Phys. Chem. Chem. Phys.*, 2019, **21**, 7239–7255.
26 J. Narayanan SJ, D. Tripathi and A. K. Dutta, *J. Chem. Phys. Lett.*, 2021, **12**, 10380–10387.
27 D. H. Kang, J. Kim, H. J. Eun and S. K. Kim, *J. Am. Chem. Soc.*, 2022, **144**, 16077–16085.
28 M. Baca, G. E. Borgstahl, M. Boissinot, P. M. Burke, D. R. Williams, K. A. Slater and E. D. Getzoff, *Biochemistry*, 1994, **33**, 14369–14377.
29 U. K. Genick, S. M. Soltis, P. Kuhn, I. L. Canestrelli and E. D. Getzoff, *Nat.*, 1998, **392**, 206–209.
30 R. Y. Tsien, *Annu. Rev. Biochem.*, 1998, **67**, 509–544.
31 M. Zimmer, *Chem. Rev.*, 2002, **102**, 759–782.
32 R. N. Day and M. W. Davidson, *Chem. Soc. Rev.*, 2009, **38**, 2887–2921.
33 D. M. Chudakov, M. V. Matz, S. Lukyanov and K. A. Lukyanov, *Physiol. Rev.*, 2010, **90**, 1103–1163.
34 V. Helms, C. Winstead and P. Langhoff, *J. Mol. Struct.*, 2000, **506**, 179–189.
35 S. B. Nielsen, A. Lapierre, J. U. Andersen, U. Pedersen, S. Tomita and L. Andersen, *Phys. Rev. Lett.*, 2001, **87**, 228102.
36 A. Svendsen, H. V. Kiefer, H. B. Pedersen, A. V. Bochenkova and L. H. Andersen, *J. Am. Chem. Soc.*, 2017, **139**, 8766–8771.
37 W. Zagorec-Marks, M. M. Foreman, J. R. Verlet and J. M. Weber, *J. Chem. Phys. Lett.*, 2019, **10**, 7817–7822.
38 L. H. Andersen, A. P. Rasmussen, H. B. Pedersen, O. B. Beletsan and A. V. Bochenkova, *J. Chem. Phys. Lett.*, 2023, **14**, 6395–6401.
39 A. P. Rasmusssen, H. B. Pedersen and L. H. Andersen, *Phys. Chem. Chem. Phys.*, 2023, **25**, 32868–32874.
40 T. T. Lindkvist, I. Djavani-Tabrizi, L. H. Andersen and S. B. Nielsen, *Phys. Rev. Lett.*, 2025, **134**, 093001.
41 Y. Toker, D. B. Rahbek, B. Klærke, A. Bochenkova and L. H. Andersen, *Phys. Rev. Lett.*, 2012, **109**, 128101.
42 A. V. Bochenkova, B. Klærke, D. B. Rahbek, J. Rajput, Y. Toker and L. H. Andersen, *Angew. Chem., Int. Ed.*, 2014, **53**, 9797–9801.
43 H. B. Pedersen, H. Juul, F. K. Mikkelsen, A. P. Rasmussen and L. H. Andersen, *Phys. Rev. A*, 2022, **106**, 053111.
44 L. H. Andersen, A. P. Rasmussen, H. B. Pedersen and N. Klinkby, *Phys. Rev. Lett.*, 2025, **134**, 193002.
45 J.-D. Chai and M. Head-Gordon, *Phys. Chem. Chem. Phys.*, 2008, **10**, 6615–6620.
46 T. H. Dunning Jr, *J. Chem. Phys.*, 1989, **90**, 1007–1023.
47 H. B. Pedersen, A. Svendsen, L. S. Harbo, H. V. Kiefer, H. Kjeldsen, L. Lammich, Y. Toker and L. H. Andersen, *Rev. Sci. Instrum.*, 2015, **86**, 063107.
48 H. V. Kiefer, E. Gruber, J. Langeland, P. A. Kusochek, A. V. Bochenkova and L. H. Andersen, *Nat. Commun.*, 2019, **10**, 1210.
49 H.-T. Liu, C.-G. Ning, D.-L. Huang, P. D. Dau and L.-S. Wang, *Angew. Chem., Int. Ed.*, 2013, **52**, 8976–8979.
50 G.-Z. Zhu, C.-H. Qian and L.-S. Wang, *J. Chem. Phys.*, 2018, **149**, 164301.
51 D.-F. Yuan, Y. Liu, C.-H. Qian, Y.-R. Zhang, B. M. Rubenstein and L.-S. Wang, *Phys. Rev. Lett.*, 2020, **125**, 073003.
52 D. H. Kang, S. An and S. K. Kim, *Phys. Rev. Lett.*, 2020, **125**, 093001.
53 M. J. Frisch, G. W. Trucks, H. B. Schlegel, G. E. Scuseria, M. A. Robb, J. R. Cheeseman, G. Scalmani, V. Barone, G. A. Petersson, H. Nakatsuji, X. Li, M. Caricato, A. V. Marenich, J. Bloino, B. G. Janesko, R. Gomperts, B. Mennucci, H. P. Hratchian, J. V. Ortiz, A. F. Izmaylov, J. L. Sonnenberg, D. Williams-Young, F. Ding, F. Lipparini, F. Egidi, J. Goings, B. Peng, A. Petrone, T. Henderson, D. Ranasinghe, V. G. Zakrzewski, J. Gao, N. Rega, G. Zheng, W. Liang, M. Hada, M. Ehara, K. Toyota, R. Fukuda, J. Hasegawa, M. Ishida, T. Nakajima, Y. Honda, O. Kitao, H. Nakai, T. Vreven, K. Throssell, J. A. Montgomery Jr., J. E. Peralta, F. Ogliaro, M. J. Bearpark, J. J. Heyd, E. N. Brothers, K. N. Kudin, V. N. Staroverov, T. A. Keith, R. Kobayashi, J. Normand, K. Raghavachari, A. P. Rendell, J. C. Burant, S. S. Iyengar, J. Tomasi, M. Cossi, J. M. Millam, M. Klene, C. Adamo, R. Cammi, J. W. Ochterski, R. L. Martin, K. Morokuma, O. Farkas, J. B. Foresman and D. J. Fox, *Gaussian 16 Revision C.01*, Gaussian Inc., Wallingford CT, 2016.
54 CCCBDB listing of precalculated vibrational scaling factors, https://cccbdb.nist.gov/vibscalejustx.asp, [Accessed 25-Aug-2025].
55 W. Skomorowski, S. Gulania and A. I. Krylov, *Phys. Chem. Chem. Phys.*, 2018, **20**, 4805–4817.
56 T. J. Santaloci and R. C. Fortenberry, *Chemistry*, 2021, **3**, 296–313.
57 A. G. S. Lauridsen, A. P. Rasmussen, N. Klinkby and L. H. Andersen, *Phys. Chem. Chem. Phys.*, 2025, **27**, 17686–17691.
58 J. Dezalay, E. K. Ashworth, J. E. Fulker, M. H. Stockett, J. A. Noble and J. N. Bull, *Phys. Chem. Chem. Phys.*, 2025, **27**, 16738–16743.
59 T. T. Lindkvist, A. P. Rasmussen, N. Klinkby, L. H. Andersen and S. B. Nielsen, *J. Chem. Phys. Lett.*, 2025, **16**, 13277–13283.